actuators

MDPI

Article

Position Control of Pump-Controlled Hydraulic Die Cushions Based on Dead-Zone Inverse Compensation and Improved Active Disturbance Rejection Control

Song He [1], Zhikui Dong [1,2,3,*], Zeyang Meng [1], Huijiang An [2,3], Kaiming Zang [1], Yi Liao [1], Guishan Yan [2], Chao Ai [1,2] and Haiwu Zheng [4]

[1] School of Mechanical Engineering, Yanshan University, Qinhuangdao 066004, China; hs@stumail.ysu.edu.cn (S.H.); mzy021115@stumail.ysu.edu.cn (Z.M.); 13171725531@163.com (K.Z.); yiliao@stumail.ysu.edu.cn (Y.L.); aichao@ysu.edu.cn (C.A.)
[2] School of Mechanical and Electrical Engineering, Xinjiang Institute of Engineering, Urumqi 830023, China; anhuijiang@xjie.edu.cn (H.A.); ygs@xjie.edu.cn (G.Y.)
[3] Xinjiang Coal Mine Electromechanical Engineering Technology Research Center, Xinjiang Institute of Engineering, Urumqi 830023, China
[4] Yanshan University Science Park, Yanshan University, Qinhuangdao 066004, China; zhw@ysu.edu.cn
* Correspondence: dzk@ysu.edu.cn

Abstract

Pump-controlled hydraulic die cushions offer energy-efficient actuation, but accurate position control is challenged by flow dead-zone nonlinearity, parameter perturbations, and external load disturbances. This study proposes a coordinated dead-zone inverse compensation (DIC) and improved active disturbance rejection control (IADRC) strategy, termed DIC-IADRC. A mechanism-based dead-zone model is derived by considering leakage across multiple piston-pump friction pairs and oil compressibility. A smooth inverse compensator is constructed using experimentally identified parameters, and its compensation error is explicitly introduced into a high-order sliding mode observer (HOSMO) as a known input for finite-time disturbance estimation. The improved ADRC further incorporates a full-range fast tracking differentiator (FFTD) and nonlinear state error feedback (NLSEF) to suppress differentiation chattering and balance response speed and smoothness. The strategy is evaluated on a physical pump-controlled hydraulic die-cushion test bench through step tracking, sudden-load disturbance rejection, and sinusoidal tracking experiments, with PID, standard ADRC, and DIC-ADRC as benchmarks. Compared with PID, DIC-IADRC reduces step overshoot by 79.4%, steady-state mean absolute error (MAE) by 83.6%, peak sudden-load tracking error by 64.9%, and maximum sinusoidal tracking deviation by 35.7%. It also outperforms standard ADRC and DIC-ADRC across the tested operating conditions.

Keywords: position control; improved active disturbance rejection control; dead-zone inverse compensation; hydraulic die cushions; pump-controlled system

Check for updates

Academic Editor: Guanghong Yang

Received: 22 October 2026
Revised: 13 November 2026
Accepted: 15 November 2026
Published: 17 November 2026

Copyright: © 2026 by the authors. Licensee MDPI, Basel, Switzerland. This article is an open access article distributed under the terms and conditions of the Creative Commons Attribution (CC BY) license.

1. Introduction

The hydraulic die cushion is a key actuator in modern stamping equipment for automobile panels. Position-control accuracy during the pre-acceleration stage directly determines the magnitude of the die-closing impact, which in turn affects forming quality and die life [1–3]. Driven by the trend toward energy conservation and carbon reduction, pump-controlled electro-hydraulic servo systems based on displacement control are gradually replacing conventional valve-controlled schemes owing to their high energy efficiency and are becoming the dominant drive configuration for hydraulic die cushions [4–6].

However, during the pre-acceleration stage, the system still exhibits significant coupling of nonlinearities and uncertainties [7]. Due to the combined effects of internal leakage in the piston pump, oil compressibility, and mechanical friction, the system is prone to a flow dead zone in the small-signal input range, causing response lag and position tracking errors in the actuator [8,9]. Meanwhile, hydraulic parameters—including the effective bulk modulus and leakage coefficients—are subject to temporal variation, while external loads fluctuate stochastically; these coupled effects compound dynamic uncertainty and undermine both position-tracking accuracy and robustness [10,11].

For the position regulation of pump-controlled electro-hydraulic systems, several advanced control strategies have been investigated, including adaptive control [12,13], sliding-mode control [14,15], and backstepping control [16]. Ahn et al. [17], Chen et al. [18], and Kim et al. [19] developed adaptive backstepping controllers for electro-hydraulic actuators and pump-controlled servo systems. These methods combine backstepping control laws with adaptive mechanisms to compensate for system nonlinearities and uncertainties, and their effectiveness has been demonstrated experimentally. Yang et al. [20] proposed an observer-based motion-axis control method for hydraulic actuation systems. Qin et al. [21] developed an adaptive robust impedance-control method for hydraulic excavator boom and stick systems, while Yang et al. [22] investigated precision motion control under unknown time-varying parameters and disturbances. Nevertheless, these methods still fundamentally rely on the accuracy of parameter estimation, uncertainty bounds, or system structural constraints; under the coupled action of strong nonlinear flow dead zone and composite disturbances, their robustness and control accuracy remain limited.

ADRC employs an extended state observer (ESO) to estimate the lumped disturbance, which includes both internal system uncertainties and external disturbances, in real time and compensate for its effects. This reduces the dependence on an accurate system model. ADRC has been applied to electro-hydraulic and hydraulic robotic systems [23,24], while Huang and Xue [25] provided a systematic analysis of its methodology and theoretical foundations. However, in pump-controlled hydraulic systems, due to the pronounced flow dead-zone nonlinearity, linear ADRC has difficulty balancing convergence speed and estimation accuracy under complex operating conditions [26,27]; although nonlinear ADRC offers greater control capability, it essentially still treats the flow dead zone as an unknown disturbance, without exploiting its known nonlinear structural characteristics for targeted compensation, and control quality degrades under strong nonlinear effects [28].

It should be noted that the above disturbance-observer-based control methods fail to distinguish the structural nonlinearity of the flow dead zone from general random disturbances, making it difficult to achieve satisfactory control performance under dead-zone-dominated operating conditions.

Meanwhile, several studies have investigated dead-zone compensation. Jiang et al. [29] characterized the low-speed dead-zone problem of electro-hydrostatic actuators by summarizing nonlinear dead-zone characteristics through experiments and constructing an adaptive compensation function, which significantly reduced dead-zone trajectory tracking errors. Wang et al. [30] proposed a control strategy combining adaptive backstepping sliding mode control with DIC for an electro-hydraulic servo closed pump-controlled system, achieving high steady-state control accuracy. Yang et al. [31] proposed an ADRC-based super-twisting integral sliding mode control method for the high-speed on/off valve dead-zone nonlinearity of a foldable airbag-driven wrist rehabilitation robot. Although these studies have made notable progress in dead-zone compensation, their controller designs are mostly based on simplified models and fail to fully account for the effects of composite factors such as external load disturbances and time-varying parameters on position-control performance. Zhao et al. [32] proposed a funnel-based predefined-time fuzzy adaptive

event-triggered control strategy for heterogeneous vehicle platoons, combining state observation, fuzzy approximation, and backstepping to handle nonlinear uncertainties and external disturbances. Similar to the present study, their method employs observer-based feedback to improve tracking performance. However, their work focuses on vehicle-spacing constraints and communication efficiency, whereas this study addresses flow dead-zone compensation and residual disturbance rejection in pump-controlled hydraulic systems through DIC and IADRC.

These limitations are particularly important during the pre-acceleration stage of a pump-controlled hydraulic die cushion. At low pump speeds, the pump output flow may be consumed by internal leakage and oil compression before overcoming the load pressure, resulting in delayed cylinder motion and position tracking errors. DIC can compensate for this identifiable flow dead-zone nonlinearity; however, variations in hydraulic parameters, external load disturbances, and unmodeled dynamics may still cause residual errors. Conversely, ADRC can estimate and reject lumped disturbances, but treating the flow dead zone solely as an unknown disturbance does not fully exploit its known nonlinear characteristics. Therefore, this study combines DIC with IADRC, in which DIC compensates for the structural dead-zone nonlinearity, while the HOSMO accounts for the compensation error as a known input and estimates the remaining lumped disturbance. The proposed DIC-IADRC is evaluated against PID, standard ADRC, and DIC-ADRC through step-tracking, sudden-load disturbance rejection, and sinusoidal-tracking experiments. The main contributions are as follows:

(1) For low-speed operating conditions of the piston pump, the generation mechanism of the flow dead zone is analyzed. A mathematical model of the dead-zone width is established by comprehensively considering leakage across multiple friction pairs and oil compressibility in the high-pressure chamber, clarifying the influence of the leakage coefficient, load pressure, chamber volume, and pump displacement on the dead-zone width.
(2) To address the problem that conventional dead-zone inverse functions are discontinuous at switching boundaries and prone to chattering, a continuously differentiable dead-zone inverse compensator based on a smooth indicator function is constructed. Dead-zone parameters are identified through open-loop experiments to achieve smooth feedforward compensation of the input-side nonlinear dead zone.
(3) To overcome the parameter-perturbation sensitivity of the conventional ESO and the chattering of nonlinear tracking differentiators, an IADRC scheme that integrates an FFTD, an HOSMO, and an NLSEF law is developed, enhancing both total-disturbance estimation accuracy and dynamic response quality.
(4) A series-coordinated control framework that couples DIC with IADRC is developed. The compensation error between the actual dead-zone characteristic and the smooth inverse model is explicitly introduced into the HOSMO as a known input, so that DIC compensates the structural dead-zone nonlinearity while the HOSMO estimates the remaining composite disturbance in finite time. The framework is validated by comparative experiments across several operating conditions: step tracking, sudden-load rejection, and sinusoidal tracking.

The remainder of the paper follows the controller-development workflow: Section 2 derives the hydraulic model and dead-zone mechanism; Section 3 formulates the DIC-IADRC architecture; Section 4 evaluates it on the physical test bench; and Section 5 summarizes the main findings.

2. System Modeling and Problem Formulation

Figure 1 depicts the overall configuration of the pump-controlled hydraulic die cushion: the left panel shows the mechanical layout and the right panel the hydraulic circuit diagram.

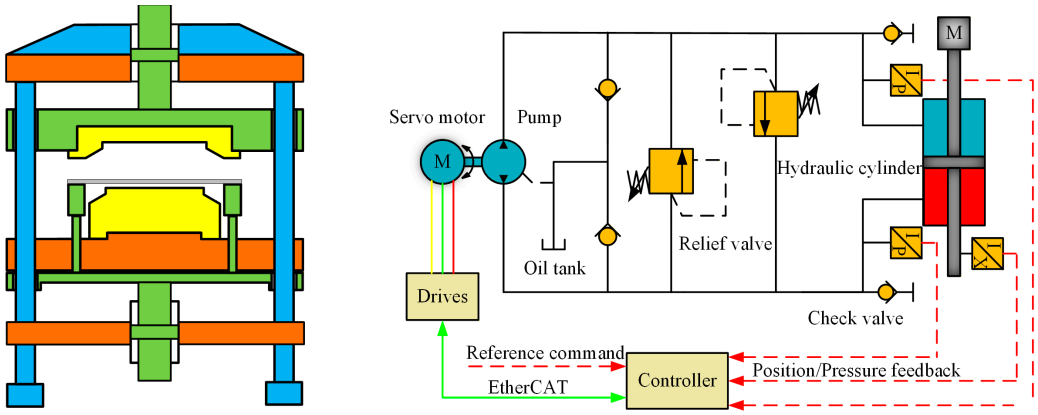


Figure 1. Configuration and hydraulic circuit diagram of the pump-controlled hydraulic die cushion.

Its principal components include a symmetric double-rod hydraulic cylinder, a bidirectional fixed-displacement piston pump driven by a servo motor, two relief valves, and two check valves. The controller receives position commands from the host computer via EtherCAT and, based on displacement sensor feedback, controls the servo motor speed and direction to drive the pump, delivering the required flow for high-accuracy position regulation of the hydraulic cylinder. Overpressure protection is ensured by relief valves installed on both sides.

2.1. Hydraulic Cylinder Mathematical Model

A double-rod double-acting hydraulic cylinder serves as the actuator. With internal/external leakage and nonlinear friction considered, the dynamic model is established, and the corresponding flow-continuity and force-balance analysis are illustrated in Figure 2.

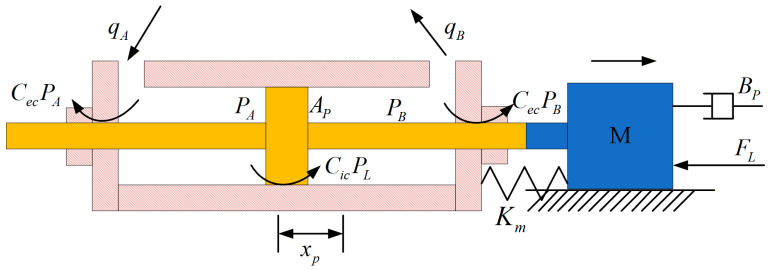


Figure 2. Flow continuity and force balance analysis of the hydraulic cylinder.

The continuity equations for the two chambers of the cylinder are given by

$$\begin{cases} q_L = A_p \frac{dx_p}{dt} + C_{tc} p_L + \frac{V_t}{4\beta_e} \frac{dp_L}{dt} \\ C_{tc} = C_{ic} + \frac{C_{ec}}{2} \end{cases} \quad (1)$$

where A_p is the piston effective area; x_p is the die cushion displacement; β_e is the effective bulk modulus, defined as the pressure increment required to produce a unit relative volume reduction in the hydraulic chamber; $p_L = p_A - p_B$ is the pressure difference across the two chambers; C_{ic} and C_{ec} are the internal and external leakage coefficients, respectively; C_{tc} is the total leakage coefficient of the cylinder; and V_t is the total compressed volume.

The force balance equation between the cylinder output and the load can be expressed as

$$A_p p_L = m_t \dot{x}_p + B_p \ddot{x}_p + F_L + K_m x_p + F_f + n\left(x_p, \frac{dx_p}{dt}, t\right) \tag{2}$$

where m_t is the equivalent total mass of the piston and load; B_P is the viscous damping coefficient of the piston and load, representing the equivalent viscous resistance, and is empirically selected based on engineering experience; F_L is the external load force acting on the hydraulic cylinder; F_f is the friction force; K_m is the equivalent stiffness of the mechanical load and the sheet metal; and $n(\cdot)$ represents lumped uncertainties and nonlinearities caused by external disturbances, unmodeled friction, and other terms that are difficult to model.

2.2. Fixed-Displacement Piston Pump Mathematical Model

The bidirectional fixed-displacement piston pump serves as the hydraulic power source. Its pressure–flow characteristics are illustrated in Figure 3.

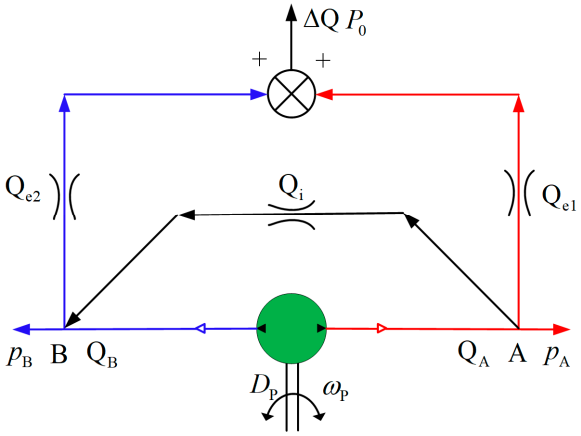


Figure 3. Pressure-flow characteristics of the bidirectional fixed-displacement pump.

The flow rates at the two pump ports are written as

$$\begin{cases} Q_A = D_p\omega_p - C_{ip}(p_A - p_B) - C_{ep}(p_A - p_0) \\ Q_B = D_p\omega_p - C_{ip}(p_A - p_B) + C_{ep}(p_B - p_0) \end{cases} \tag{3}$$

where ω_P is the pump rotational speed; D_p is the pump displacement; C_{ep} and C_{ip} denote the external and internal leakage coefficients, respectively; Q_A and Q_B are the output flow rates at ports A and B; p_A and p_B denote the pressures at pump ports A and B, respectively; and p_0 denotes the tank (reference) pressure.

Combining these two equations yields the load flow continuity equation:

$$q_L = D_p\omega_p - C_{tp}p_L \tag{4}$$

where $C_{tp} = C_{ip} + \frac{C_{ep}}{2}$ is the total leakage coefficient of the pump, and q_L denotes the load flow supplied by the pump to the hydraulic cylinder.

2.3. Servo Motor Mathematical Model

The drive element is a surface-mounted permanent-magnet synchronous motor (SPMSM), modeled in the synchronous rotating d–q frame.

The motor's mechanical equation of motion is

$$T_e - T_L = J_m\frac{d\omega_m}{dt} + B_m\omega_m \tag{5}$$

where B_m is the rotational damping coefficient, and is empirically selected based on engineering experience; J_m is the equivalent inertia reflected to the motor shaft; $T_L = D_p p_L$ represents the load torque exerted on the motor shaft; T_e is the motor electromagnetic torque; and ω_m denotes the motor mechanical angular velocity.

For the SPMSM, the electromagnetic torque is proportional to the q-axis current as follows:

$$T_e = 1.5 p_n \psi_f i_q \tag{6}$$

where ψ_f represents the permanent-magnet flux linkage; p_n gives the number of pole pairs; and i_q is the q-axis component of the stator current. Therefore, the electromagnetic torque can be linearly regulated by controlling i_q.

As the current and speed loops of the servo motor have a considerably higher bandwidth than the hydraulic system, the motor can be modeled as a simple gain for system-level analysis:

$$\omega_p = K_u u_m(t) \tag{7}$$

where $u_m(t)$ is the control voltage, and K_u is the gain coefficient.

2.4. Flow Dead-Zone Mechanism and Model

2.4.1. Dead-Zone Generation Mechanism

In the position control system of the pump-controlled hydraulic die cushion, due to the coupled effects of piston pump internal leakage, oil compressibility, and friction, the system cannot deliver effective flow under small input signals, producing a "flow dead zone" that seriously degrades low-speed position control accuracy.

Taking a closed-circuit system driven by a bidirectional fixed-displacement piston pump as an example, the startup process of the hydraulic cylinder is divided into two stages: the pressure build-up stage and the effective flow output stage. During the pressure build-up stage, the servo motor drives the piston pump to supply oil to the high-pressure chamber V_h, but the entire output flow is consumed to compensate for system leakage ΔQ and oil compression Q_c. Therefore, the effective output flow remains zero, i.e., $Q_p = 0$; then,

$$D_p \omega_p = Q_p + \Delta Q + Q_c \tag{8}$$

Here, Q_p denotes the effective output flow delivered by the pump; ΔQ represents the internal leakage flow; and Q_c denotes the compression flow consumed by oil compression in the high-pressure chamber.

Only after the pump outlet pressure p_p overcomes the load pressure p_L does the system enter the second stage and begin to deliver effective flow to drive the hydraulic cylinder. The range of motor speed from startup to the onset of cylinder displacement constitutes the flow dead-zone width.

2.4.2. Dead-Zone Flow Characteristic Model

Piston-pump internal leakage originates primarily from three frictional interfaces—the piston–cylinder, slipper, and valve plate pairs. Because oil viscosity is temperature-dependent, the total leakage coefficient C_{ip} is expressed as

$$\begin{aligned} C_{ip} &= C_{ip1} + C_{ip2} + C_{ip3} \\ &= \frac{1}{12\mu_0 e^{-\alpha(T-T_0)}} \left[\frac{\pi d \delta_1^3 (1+1.5\varepsilon^2)}{l} + \frac{2\pi d_4^4 \delta_3^3}{d_1^4 \ln(r_2/r_1) + 128 l_1 \delta_2^3} + \left(\frac{\alpha_f \delta_3^3}{\ln(R_2/R_1)} + \frac{\alpha_f \delta_3^3}{\ln(R_4/R_3)} \right) \right] \end{aligned} \tag{9}$$

where μ_0 is the dynamic viscosity of the oil, α is the viscosity-temperature coefficient, T is the oil temperature, δ_1,δ_2,δ_3 are the oil film clearances of the piston/cylinder pair, slipper pair, and valve plate pair, respectively; the remaining symbols are structural parameters of

each friction pair. The symbols d, d_1 and d_4 denote the characteristic diameters of the corresponding friction-pair geometries; l and l_1 represent the associated leakage-path lengths; r_1 and r_2 denote the inner and outer radii of the corresponding annular leakage passage; R_1, R_2, R_3, and R_4 represent the radii defining the two annular leakage passages; ε is the eccentricity ratio of the piston–cylinder pair; and α_f is the geometric coefficient associated with the valve-plate leakage model.

Therefore, the mathematical model of piston pump leakage flow is

$$\Delta Q = C_{ip} p_p \tag{10}$$

Here, p_p denotes the pump outlet pressure, which corresponds to the pressure in the high-pressure chamber during the pressure-build-up stage.

The compression flow in the high-pressure chamber is

$$Q_c = \frac{V_h}{\beta_e} \frac{\mathrm{d}p_p}{\mathrm{d}t} \tag{11}$$

Here, V_h denotes the effective volume of the high-pressure chamber.

From flow conservation, the total flow continuity equation of the piston pump is

$$D_p \omega_p = Q_p + C_{ip} p_p + \frac{V_h}{\beta_e} \frac{\mathrm{d}p_p}{\mathrm{d}t} \tag{12}$$

When the system enters the second stage of startup, the pump outlet pressure rises to the load pressure p_L, and Equation (12) can be written as

$$D_p \omega_p = Q_p + C_{ip} p_L + \frac{V_h}{\beta_e} \frac{\mathrm{d}p_L}{\mathrm{d}t} \tag{13}$$

Let t_0 be the instant at which the piston pump begins to deliver effective flow, at which $Q_p = 0$, $\omega_p(t_0) = n_0$. Solving Equation (13) for the rotational speed yields

$$\omega_p = \frac{C_{ip}}{D_p} p_L + \frac{V_h}{D_p \beta_e} \frac{\mathrm{d}p_L}{\mathrm{d}t} \tag{14}$$

Substituting the boundary conditions, the unidirectional flow dead-zone width is obtained as

$$n_0 = \frac{C_{ip}}{D_p} p_L + \left. \frac{V_h}{D_p \beta_e} \frac{\mathrm{d}p_L}{\mathrm{d}t} \right|_{t=t_0} \tag{15}$$

Equation (15) provides a theoretical basis for qualitatively analyzing the effects of leakage, load pressure, oil compressibility, and chamber volume on the flow dead-zone characteristics. The actual dead-zone parameters are subsequently determined through experimental identification rather than direct calculation from Equation (15).

In Equation (15), the first term represents the rotational speed required to compensate for leakage, and the second term represents that required to compensate for oil compression.

The dead-zone range of the bidirectional piston pump is $[-n_0 \sim n_0]$, with a width of $2n_0$. As indicated by Equation (15), the dead-zone width increases with the leakage coefficient C_{ip}, the load pressure P_L, and the high-pressure chamber volume V_h, while it decreases with the pump displacement D_p. Moreover, an increase in oil temperature reduces the oil viscosity, leading to a larger C_{ip} and thereby indirectly widening the dead zone.

2.5. State-Space Model

By combining Equations (1), (2), and (4) and applying the Laplace transform, the state variable is selected as $\mathbf{x} = [x_1, x_2, x_3]^T = \left[x_p, \dot{x}_p, \ddot{x}_p\right]^T$. The state-space equation of the system is established as follows:

$$\begin{cases} \dot{x}_1 = x_2 \\ \dot{x}_2 = x_3 \\ \dot{x}_3 = -\frac{4\beta_e C_t K_m}{V_t m_t} x_1 - \frac{4\beta_e A_p^2 + 4\beta_e C_t B_p + V_t K_m}{V_t m_t} x_2 \\ -\frac{4\beta_e C_t m_t + V_t B_p}{V_t m_t} x_3 + \frac{4\beta_e A_p D_p}{V_t m_t} u_0 - \frac{4\beta_e C_t}{V_t m_t} d - \frac{1}{m_t} \dot{d} \end{cases} \tag{16}$$

where x_1, x_2, and x_3 represent the hydraulic cylinder displacement, velocity, and acceleration, respectively; $C_t = C_{tc} + C_{tp}$ is the overall leakage coefficient of the system, $d = F_L + F_f + n\left(x_p, \dot{x}_p, t\right)$; and u_0 denotes the equivalent pump-speed control command generated by the ADRC for position control of the pump-controlled hydraulic die cushion.

3. Controller Design

3.1. Overall Controller Structure

To cope with the flow dead zone, parameter uncertainty, and external load disturbances of the pump-controlled hydraulic die cushion, an IADRC scheme incorporating dead-zone inverse compensation is developed; its overall architecture is depicted in Figure 4.

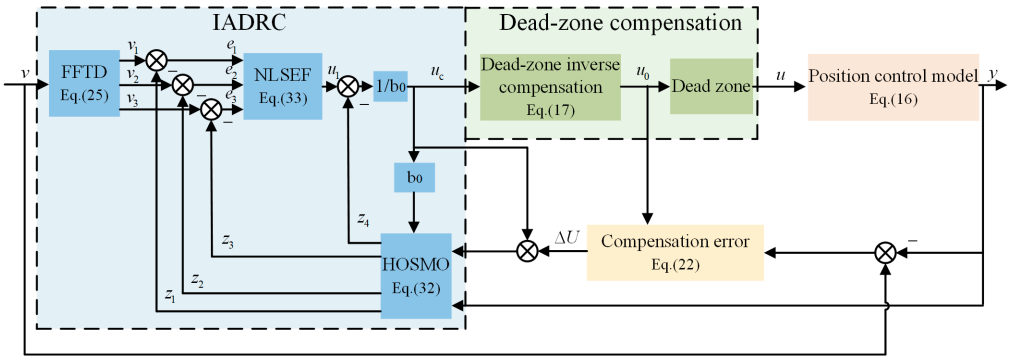


Figure 4. Structure of DIC-IADRC.

The controller comprises a dead-zone inverse compensator and an IADRC in series. The former constructs a smooth inverse function from experimentally identified dead-zone parameters to pre-compensate the flow dead zone, approximately linearizing the input nonlinearity. The compensation error caused by the mismatch between the actual dead-zone characteristic and the smooth inverse model is then explicitly introduced into the HOSMO as a known input. The FFTD shapes the reference trajectory to obtain smooth reference signals, the HOSMO estimates the system states and the remaining lumped disturbance in real time, and the NLSEF generates the error feedback, which is combined with disturbance feedforward and passed through the dead-zone inverse compensator to drive the servo motor–pump unit. The two parts act cooperatively—DIC compensates the structural dead-zone nonlinearity, while the HOSMO rejects the remaining composite disturbance—jointly improving position control accuracy and robustness.

3.2. Dead-Zone Inverse Compensator Design

During position control of the pump-controlled hydraulic die cushion, a flow dead zone occurs when the piston pump operates at low speed or reverses its direction. Conventional nonlinear dead-zone inverse functions are prone to chattering.

Therefore, a dead-zone inverse compensation method based on smooth continuous indicator functions is adopted to construct a continuously differentiable smooth dead-zone inverse function:

$$u_0 = \frac{u_c + \hat{m}_r \hat{b}_r}{\hat{m}_r} \varphi_r(u_c) + \frac{u_c + \hat{m}_l \hat{b}_l}{\hat{m}_l} \varphi_l(u_c) \tag{17}$$

where the smooth compensation functions $\varphi_r(u_c)$ and $\varphi_l(u_c)$ are defined as

$$\begin{cases} \varphi_r(u_c) = \frac{e^{u_c/\sigma}}{e^{u_c/\sigma} + e^{-u_c/\sigma}} \\ \varphi_l(u_c) = \frac{e^{-u_c/\sigma}}{e^{u_c/\sigma} + e^{-u_c/\sigma}} \end{cases} \tag{18}$$

Here, $\hat{m}_r$, $\hat{m}_l$, $\hat{b}_r$ and $\hat{b}_l$ are the estimated dead-zone parameters identified from the hydraulic die-cushion position-control experiments, and $\sigma > 0$ is an adjustable smoothing parameter, u_0 is the pre-compensated pump-speed command generated by the dead-zone inverse compensator and applied to the servo motor–pump unit, u_c denotes the control command generated by the ADRC before dead-zone inverse compensation.

To obtain the dead-zone parameter estimates, the overall dead-zone characteristics of the system were measured on the experimental platform. The loading system was set to provide an external load force of 10 kN, and the servo motor was controlled to drive the hydraulic cylinder to extend or retract in increments/decrements of 2.5 r/min. The relationship between the input rotational speed and the cylinder displacement was recorded, yielding the overall dead-zone curves in the positive and negative directions, as shown in Figure 5. The estimated dead-zone parameters obtained from the figure are $\hat{b}_r = 36.71$ r/min, $\hat{b}_l = -35.28$ r/min, $\hat{m}_r = 0.0022$ m/(r/min), and $\hat{m}_l = 0.0024$ m/(r/min).

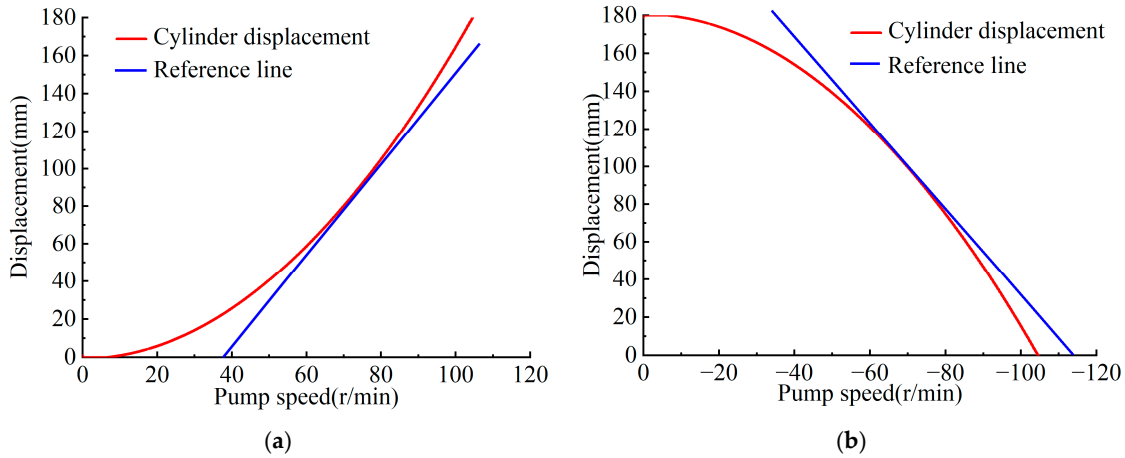


Figure 5. Relationship between input speed and hydraulic cylinder displacement. (**a**) Forward dead-zone curve; (**b**) reverse dead-zone curve.

The identified dead-zone parameters correspond to the experimental condition with a 10 kN external load and are used to construct the inverse compensator. Equation (15) serves as a qualitative explanation of the dead-zone formation mechanism rather than a quantitatively validated predictive model.

Substituting the identified parameters into Equations (17) and (18) yields the dead-zone inverse compensator. Since the true dead-zone values vary with operating conditions and differ from their estimates, a compensation error arises.

The actual dead-zone characteristic is parameterized as

$$u(t) = -\theta^T \omega(t) \tag{19}$$

where $\theta = (m_r, m_r b_r, m_l, m_l b_l)^T$, $\omega(t) = [-\gamma_r(u_0)u_0(t), \gamma_r(u_0), -\gamma_l(u_0)u_0(t), \gamma_l(u_0)]^T$.

The indicator functions $\gamma_r(t)$ and $\gamma_l(t)$ are defined as

$$\gamma_r(t) = \begin{cases} 1, & u(t) \geq 0 \\ 0, & u(t) < 0 \end{cases}, \qquad \gamma_l(t) = \begin{cases} 1, & u(t) \leq 0 \\ 0, & u(t) > 0 \end{cases} \tag{20}$$

The vector θ contains the actual dead-zone parameters, and $\omega(t)$ is the corresponding regressor vector. The functions $\gamma_r(t)$ and $\gamma_l(t)$ are binary indicator functions that identify the forward and reverse operating branches, respectively, according to the sign of $u(t)$.

Based on the identified dead-zone parameters, the output of the smooth dead-zone inverse model is expressed as

$$u_d(t) = -\hat{\theta}^T \hat{\omega}(t) \tag{21}$$

where $\hat{\theta}$ is the estimate of θ, i.e., $\hat{\theta} = \left(\hat{m}_r, \hat{m}_r\hat{b}_r, \hat{m}_l, \hat{m}_l\hat{b}_l\right)^T$ and $\hat{\omega}$ is the estimate of ω, given by $\hat{\omega}(t) = [-\varphi_r(u_0)u_0(t), \varphi_r(u_0), -\varphi_l(u_0)u_0(t), \varphi_l(u_0)]^T$.

Therefore, the compensation error between the actual dead-zone characteristic and the smooth dead-zone inverse model is

$$\Delta u(t) = u(t) - u_d(t) = \tilde{\theta}^T \hat{\omega}(t) + d_N(t) \tag{22}$$

where $\tilde{\theta} = \hat{\theta} - \theta$ denotes the dead-zone parameter estimation error, and the unmodeled deviation $d_N(t) = \theta^T[\hat{\omega}(t) - \omega(t)]$ is bounded by

$$|d_N(t)| \leq \begin{cases} \frac{\sigma|m_r - m_1|}{2\mathrm{e}} + \frac{|m_r b_r - m_1 b_1|}{\exp(2b_r/\sigma + 1)} & u_0(t) \geq b_r \\ \max\{m_r, m_l\}\,|b_r - b_l| & b_1 < u_0(t) < b_r \\ \frac{\sigma|m_r - m_1|}{2\mathrm{e}} + \frac{|m_r b_r - m_1 b_1|}{\exp(-2b_1/\sigma + 1)} & u_0(t) \leq b_1 \end{cases} \tag{23}$$

As shown by Equation (23), regardless of whether u_0 lies inside or outside the dead zone, $|d_N(t)|$ remains bounded, and its magnitude can be adjusted through σ. The transition from the dead-zone region to the effective-flow region is therefore smooth and continuous; an appropriate choice of σ improves dead-zone compensation, as well as the dynamic response and control accuracy of the system.

Since the actual dead-zone output cannot be directly measured, the unknown compensation error is treated as a disturbance to be handled by the HOSMO. Meanwhile, an online compensation signal Δu is constructed using the hydraulic cylinder position tracking error e and the pump-speed command u_0.

The compensation rules are established as follows. When $u_0 > 0$ and $e > 0$, undercompensation is indicated, requiring an increase in the control action; when $u_0 > 0$ and $e < 0$, overcompensation is indicated, requiring a reduction in the control action. When $u_0 < 0$ and $e > 0$, overcompensation is indicated, requiring a reduction in the reverse control action; when $u_0 < 0$ and $e < 0$, undercompensation is indicated, requiring an increase in the reverse control action.

Accordingly, the online compensation signal is defined as

$$\Delta u = k e \mathrm{sgn}(u_0) \tag{24}$$

where e is the cylinder position tracking error, and k is the compensation adjustment coefficient. The compensation signal Δu can be calculated online from the available signals and is introduced into the HOSMO as a known input. The remaining unknown compensation discrepancy is incorporated into the lumped disturbance.

3.3. IADRC Structure

3.3.1. Tracking Differentiator

Conventional nonlinear tracking differentiators exhibit chattering when obtaining signal derivatives. The FFTD combines nonlinear and linear terms into a continuous composite structure, retaining fast tracking while suppressing chattering.

The mathematical expression of the third-order FFTD is

$$\begin{cases} \dot{v}_1 = v_2 \\ \dot{v}_3 = R^3\Big[-a_0(v_1 - v(t)) - a_1(v_1 - v(t))^{m/n} - \rho_0\frac{v_2}{R} - \rho_1\big(\frac{v_2}{R}\big)^{m/n} - c_0\frac{v_3}{R^2} - c_1\big(\frac{v_3}{R^2}\big)^{m/n}\Big] \\ \dot{v}_2 = v_3 \end{cases} \tag{25}$$

where $v(t)$ is the input signal; v_1, v_2 and v_3 are the tracking signal and its first and second derivatives, respectively; $R > 0$ is the speed factor; a_0, ρ_0, and c_0 are linear gains; a_1, ρ_1, and c_1 are nonlinear gains, and m, n are positive odd integers with $m < n$.

When the nonlinear terms are removed, the linear part of the differentiator dominates:

$$\begin{cases} \dot{v}_1 = v_2 \\ \dot{v}_2 = v_3 \\ \dot{v}_3 = R^3\Big[-a_0(v_1 - v(t)) - \rho_0\frac{v_2}{R} - c_0\frac{v_3}{R^2}\Big] \\ v_{\text{out}} = v_3(t) \end{cases} \tag{26}$$

Here, $v_{\text{out}}(t)$ denotes the output signal of the FFTD, which is equal to the second derivative tracking signal $v_3(t)$.

3.3.2. High-Order Sliding Mode Observer

After the input-side dead-zone structure has been treated by DIC, the observer is required to reconstruct only the residual lumped disturbance and the system states. For this purpose, a HOSMO is adopted in place of the conventional ESO. Its finite-time convergence property is exploited to improve state/disturbance reconstruction under the parameter perturbations that remain in the hydraulic plant.

For an nth-order single-input single-output system:

$$\begin{cases} \dot{x}_1 = x_2 \\ \vdots \\ \dot{x}_n = f(t, x, \Delta b) + b_0 u \\ y = x_1 \end{cases} \tag{27}$$

where $f(t,x,\Delta b)$ includes internal system uncertainties, external disturbances, input-gain variations, and the remaining discrepancy between the actual dead-zone compensation effect and the constructed online compensation signal; b_1 denotes the actual system input gain, b_0 is the nominal input gain adopted in the controller design, and $\Delta b = b_1 - b_0$ denotes the input-gain deviation.

The general form of the designed high-order sliding mode observer is

$$\begin{cases} \dot{z}_1 = v_1 \\ v_1 = -\lambda_1 L^{1/(n+1)}\big|z_1 - y\big|^{n/(n+1)}\text{sign}(z_1 - y) + z_2 \\ \vdots \\ \dot{z}_n = \hat{f} + b_0 u \\ \hat{f} = -\lambda_n L^{1/2}\big|z_n - v_{n-1}\big|^{1/2}\text{sign}(z_n - v_{n-1}) + z_{n+1} \\ \dot{z}_{n+1} = -\lambda_{n+1} L\text{sign}(z_{n+1} - \hat{f}) \end{cases} \tag{28}$$

Here, z_i denotes the observer state used to estimate the corresponding system state x_i, v_i represents an auxiliary correction signal generated by the observer, λ_i denotes the positive observer gain, L is the Lipschitz constant bounding the variation in the lumped disturbance, and $\text{sgn}(\cdot)$ is the signum function.

With appropriate observer parameters λ_i, the estimates satisfy $z_i \to x_i \quad (i = 1,\ldots,n)$ and $z_{n+1} \to f$ in finite time, enabling exact estimation of the states and the total disturbance under the stated assumptions.

With the high-order sliding mode observer parameters properly selected, if the output signal $y(t)$ and input signal $u(t)$ are both bounded and Lebesgue-measurable, and in the absence of measurement noise, the system satisfies the following equalities in finite time:

$$\begin{aligned} z_i &= x_i, \quad i = 1, 2, \ldots, n \\ z_{n+1} &= f(t, x, \Delta b) \end{aligned} \tag{29}$$

Here, a recursive method is adopted to select the parameters λ_i: when $n = k$, the parameters λ_1,...,λ_k are chosen; when $n = k + 1$, these can serve as λ_2,...,λ_{k+1}, so that only a new λ_1 needs to be designed.

When the output signal $y(t)$ and input signal $u(t)$ are subject to bounded Lebesgue-measurable noise, with the noise ranges assumed to be $[-\varepsilon,\varepsilon]$ and $[-k\varepsilon^{(n-1)/n},k\varepsilon^{(n-1)/n}]$, $k > 0$, respectively, the following inequalities hold in finite time:

$$\begin{cases} |z_1 - x_1| \le \mu_1 \varepsilon \\ |z_2 - x_2| \le \mu_2 \varepsilon^{(n-1)/n} \\ \vdots \\ \left|\hat{f} - f\right| \le \mu_f \varepsilon^{1/n} \end{cases} \tag{30}$$

Here, ε denotes the measurement-noise bound, and μ_i are positive constants determined by K and the observer gains λ_i.

The mathematical model of the pump-controlled hydraulic die cushion can be simplified to third order; therefore, $n = 3$ is selected. The dead-zone compensation error Δu obtained in Equation (22) is explicitly introduced into the observer as a known input. Accordingly, the third-order system used for the observer design is written as

$$\begin{cases} \dot{x}_1 = x_2 \\ \dot{x}_2 = x_3 \\ \dot{x}_3 = f(t, x, \Delta b) + b_0(u_d + \Delta u(t)) \\ y = x_1 \end{cases} \tag{31}$$

where y is the system output (hydraulic cylinder displacement).

The corresponding HOSMO is designed as

$$\begin{cases} \dot{z}_1 = q_1 \\ q_1 = -\lambda_1 L^{1/4} |z_1 - y|^{3/4} \mathrm{sign}(z_1 - y) + z_2 \\ \dot{z}_2 = q_2 \\ q_2 = -\lambda_2 L^{1/3} |z_2 - q_1|^{2/3} \mathrm{sign}(z_2 - q_1) + z_3 \\ \dot{z}_3 = \hat{f} + b_0(u_d + \Delta u(t)) \\ \hat{f} = -\lambda_3 L^{1/2} |z_3 - q_2|^{1/2} \mathrm{sign}(z_3 - q_2) + z_4 \\ \dot{z}_4 = -\lambda_4 L \mathrm{sign}(z_4 - \hat{f}) \end{cases} \tag{32}$$

where z_1, z_2 and z_3 are the estimated cylinder displacement, velocity, and acceleration, respectively; z_4 is the observer state that converges to the remaining lumped disturbance $f(t,x,\Delta b)$, $\hat{f}$ is its real-time estimate, L is the Lipschitz constant, and λ_i are the observer gains.

3.3.3. Nonlinear State Error Feedback Control Law

Linear feedback has limited effectiveness under large disturbances and parameter variations. The NLSEF adjusts the control gain through a nonlinear function to exhibit different gain characteristics across error ranges, balancing rapidity and smoothness. Using the reference signals v_i generated by the FFTD and the state estimates z_i provided by the HOSMO, the errors are defined as $e_i = v_i - z_i$ $(i = 1,2,3)$.

The feedback control signal u_1 is then generated by combining the nonlinear function $\mathrm{fal}(\cdot)$ as follows:

$$\begin{cases} e_i = v_i - z_i \\ u_1 = k_1 \mathrm{fal}(e_1, \alpha_{21}, \delta_1) + k_2 \mathrm{fal}(e_2, \alpha_{22}, \delta_2) + k_3 \mathrm{fal}(e_3, \alpha_{23}, \delta_3) \end{cases} \tag{33}$$

where the nonlinear function $\mathrm{fal}(e,\alpha,\delta)$ is defined as:

$$\mathrm{fal}(e, \alpha, \delta) = \begin{cases} |e|^{\alpha} \mathrm{sign}(e), & |e| > \delta \\ \frac{e}{\delta^{1-\alpha}}, & |e| \le \delta \end{cases} \tag{34}$$

Here, $e_i = v_i - z_i \quad (i = 1,2,3)$ denotes the tracking error between the reference signal and the corresponding estimated state. The parameters k_i are the feedback gains, α_{2i} are the nonlinear exponents, and δ_i are the boundary-layer widths used to determine the transition between the nonlinear and linear feedback regions. The function $\mathrm{fal}(\cdot)$ provides nonlinear error-dependent feedback for large errors and a linear response within the boundary layer.

This function provides nonlinear error-dependent feedback outside the linear region and a linear response for small errors, helping to balance convergence speed and smoothness; the parameter α is typically selected such that $0 < \alpha < 1$.

Finally, the total disturbance estimated by the HOSMO is feedforward-compensated into the control law, yielding the hydraulic cylinder displacement command input to the dead-zone inverse compensator:

$$u_c = \frac{u_1 - z_4}{b_0} \tag{35}$$

where z_4 is the estimated total disturbance.

According to Equations (33) and (35), the estimated states z_1, z_2, and z_3 are used in the nonlinear state error feedback, while z_4 is used for disturbance compensation. Therefore, the observer gains influence the transient closed-loop response through their effects on estimation accuracy and noise sensitivity. The finite-time convergence and noise-related estimation bounds in Equations (29) and (30) characterize the observer performance under the corresponding assumptions, while the overall closed-loop response also depends on the nonlinear feedback control law.

3.3.4. Parameter Tuning

The parameters of the FFTD, HOSMO, and NLSEF are tuned sequentially to facilitate controller implementation. The main parameters to be tuned for the FFTD are the speed factor R and the linear gains a_0, ρ_0, and c_0. Increasing R speeds up tracking, but excessively large R introduces noise; decreasing R slows the response. When the nonlinear gains a_1, ρ_1, and c_1 are set to zero, the differentiator reduces to its linear form. After tuning, the following values are selected: $R = 100$ and $a_0 = \rho_0 = c_0 = 0.9$.

The HOSMO requires tuning of the Lipschitz constant L and the observer gains λ_i. This paper takes $L = 1$, and the gains λ_i are selected using a recursive method. The observer gains are further tuned by balancing estimation speed and noise sensitivity. Excessively large gains may amplify measurement noise and induce oscillations, whereas excessively small gains may slow down disturbance estimation and weaken disturbance compensation. Accordingly, the following values are selected: $\lambda_1 = 8$, $\lambda_2 = 5$, $\lambda_3 = 3$, and $\lambda_4 = 2$.

The NLSEF requires tuning of the error gains k_1, k_2, and k_3. k_1 is analogous to the proportional gain and affects response speed; increasing k_1 speeds up the response but can easily induce oscillation, and $k_1 = 100$ is selected. k_2 and k_3 have critical values—excessively large values cause divergence, while excessively small values cause sustained oscillation—and they are taken as $k_2 = 5$ and $k_3 = 1$.

4. Experimental Verification

4.1. Experimental Platform

As shown in Figure 6, the experimental bench operates as a closed signal-and-power chain. Position commands from a Hilectro HIC3700 master controller are sent over EtherCAT to Hilectro HI360-series servo drives, which in turn drive a Hilectro HP11318 servo motor coupled directly to the shaft of a TAKAKO TFH-040 fixed-displacement piston pump. By adjusting the pump speed, the motor controls the flow delivered to a custom Changmao Hydraulics symmetric double-rod cylinder that generates the die-cushion output force and linear displacement. A Zheda Jingyi HP-series displacement transducer and a Shanghai Zhuhong PH3601 pressure transducer feed back the cylinder position and chamber pressure to the HIC3700, closing the position and pressure loops through the EtherCAT fieldbus.

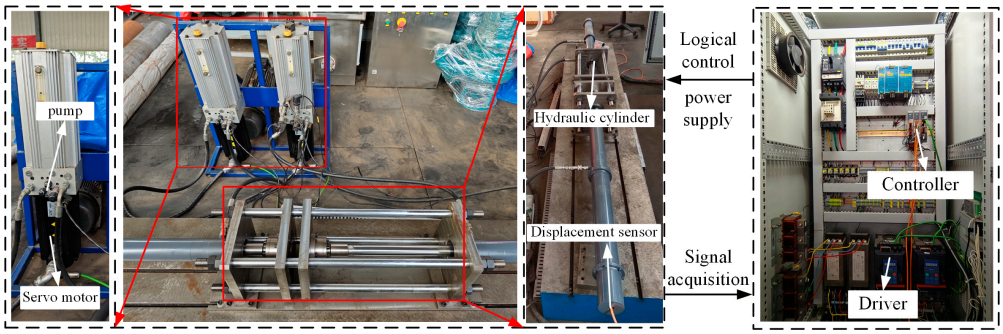


Figure 6. Experimental test bench of the pump-controlled hydraulic die cushion.

4.2. Analysis of Step Response Experiments

4.2.1. Step Tracking Experiment

To evaluate the step-tracking performance of the proposed DIC-IADRC strategy, an 80 mm step displacement command was applied. Comparative experiments were conducted using conventional PID, standard ADRC, and DIC-ADRC as benchmark controllers. Three transient metrics are considered: the rise time, i.e., the time required for the displacement to first reach the command value; the overshoot, i.e., the maximum amount by which the output displacement exceeds the command during the transient; and the settling time, i.e., the time after which the response settles within the error band. For steady-state assessment, the tracking error is quantified by its mean absolute value (MAE) and standard deviation (STD), both computed over the 4–5 s interval following complete convergence. Figure 7 plots the step-tracking curves, while Table 1 summarizes the performance metrics for all four controllers.

Table 1. Comparison of step position tracking performance metrics.

Performance Metric	PID	ADRC	DIC-ADRC	DIC-IADRC
Rise time (s)	0.409	0.374	0.369	0.362
Maximum overshoot (mm)	1.712	0.616	0.516	0.352
Settling time (s)	0.913	0.730	0.590	0.490
Steady-state MAE (mm)	0.073	0.028	0.021	0.012
Steady-state error STD (mm)	0.043	0.039	0.031	0.020

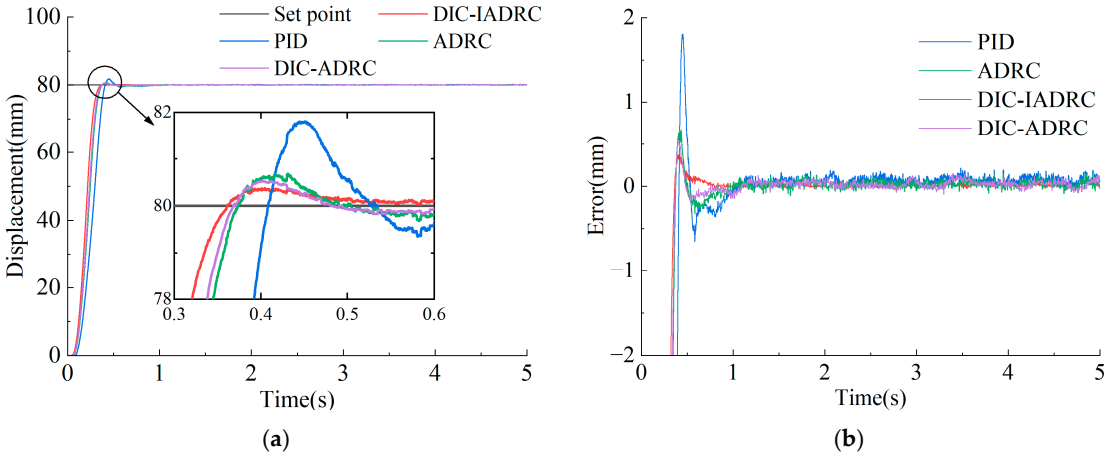


Figure 7. Step position tracking curves. (**a**) Step position tracking curve; (**b**) step position tracking error curve.

In terms of dynamic response characteristics, the dead-zone nonlinearity inherent in pump-controlled hydraulic systems creates a control input dead zone, leading to significant lag in the initial response. Conventional PID control lacks an active compensation mechanism for nonlinear elements; its step response rise time is 0.409 s, overshoot reaches 1.712 mm, and settling time is 0.913 s, exhibiting overall slow response, large overshoot, and a long transient process.

Standard ADRC estimates the total system disturbance in real time through the ESO and applies feedforward compensation, which can partially offset the lag caused by dead-zone nonlinearity. Compared with PID, ADRC reduces the rise time by 0.035 s (8.6%), overshoot by 1.096 mm (64.0%), and settling time by 0.183 s (20.0%). With the introduction of the front-end DIC, DIC-ADRC pre-compensates the dead-zone nonlinear distortion at the control input, further improving the system response. Its rise time, overshoot, and settling time are reduced to 0.369 s, 0.516 mm, and 0.590 s, respectively, representing improvements of 9.8%, 69.9%, and 35.4% compared with PID. Furthermore, DIC-IADRC achieves the best dynamic performance, with a rise time of 0.362 s, an overshoot of 0.352 mm, and a settling time of 0.490 s. Compared with PID, DIC-IADRC reduces the rise time by 11.5%, the overshoot by 79.4%, and the settling time by 46.3%.

In terms of steady-state tracking performance, dead-zone nonlinearity induces limit-cycle oscillations during the steady-state phase, which is the key factor limiting position-tracking accuracy. Conventional PID control cannot effectively suppress this nonlinear oscillation; its steady-state MAE reaches 0.073 mm and steady-state error STD is 0.043 mm. Standard ADRC relies on the disturbance rejection capability of the ESO to partially compensate for steady-state fluctuations caused by the dead zone. Compared with PID, ADRC reduces the steady-state MAE by 0.045 mm (61.6%), while the STD only decreases from 0.043 mm to 0.039 mm. The DIC-ADRC strategy further suppresses steady-state limit-cycle oscillations through DIC, reducing the MAE and STD to 0.021 mm and 0.031 mm, respectively. DIC-IADRC achieves the lowest steady-state MAE of 0.012 mm and STD of 0.020 mm, corresponding to reductions of 83.6% and 53.5% compared with PID, respectively.

4.2.2. Step Disturbance Rejection Experiment

In addition to nominal tracking accuracy, disturbance rejection is equally important for evaluating die cushion control performance. To further verify robustness, a 1 kN step external load is suddenly applied at 2.5 s while the system stably tracks the 80 mm step displacement. The maximum tracking error is defined as the maximum absolute deviation from the set value under disturbance, and the recovery time as the time from

the instant of maximum deviation until reconvergence within the steady-state error band. Figure 8 illustrates the disturbance rejection behavior, while Table 2 reports the associated performance metrics.

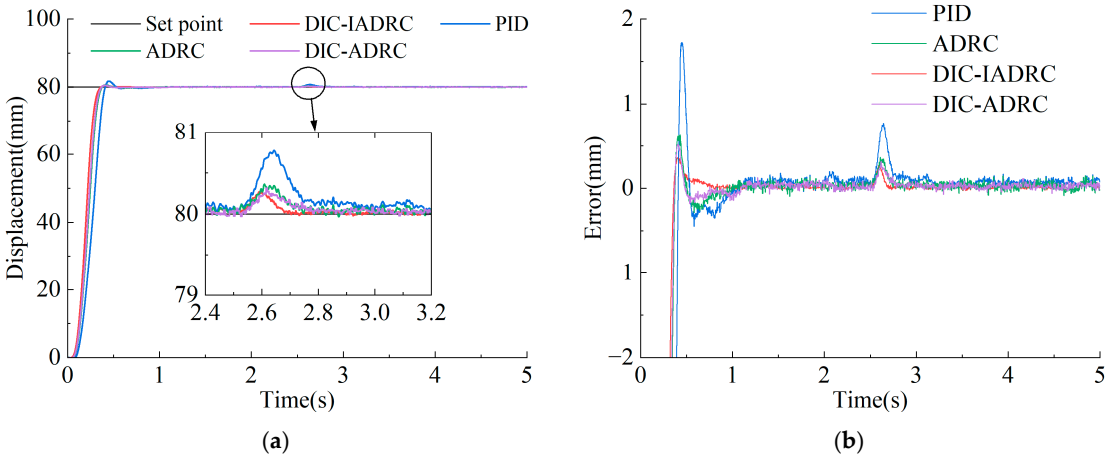


Figure 8. Step displacement disturbance rejection curves. (**a**) Step displacement disturbance rejection comparison curves; (**b**) step displacement disturbance rejection error curves.

Table 2. Comparison of step displacement disturbance rejection performance metrics.

Performance Metric	PID	ADRC	DIC-ADRC	DIC-IADRC
Max. tracking error (mm)	0.775	0.362	0.315	0.272
Max. error reduction (%)	–	53.3	59.4	64.9
Recovery time (s)	0.213	0.110	0.080	0.039
Recovery time reduction (%)	–	48.4	62.4	81.6

Because the PID controller does not account for parameter uncertainties or input nonlinearity in the pump-controlled hydraulic system, it exhibits a large position deviation under sudden load changes, with a peak tracking error of 0.775 mm and a recovery time of 0.213 s to the stable error band. In contrast, ADRC employs the ESO to estimate the total disturbance in real time and compensate for it via feedforward, effectively attenuating the disturbance impact and reducing the peak tracking error to 0.362 mm (53.3% lower than PID) and the recovery time to 0.110 s (48.4% shorter than PID). Furthermore, DIC-ADRC incorporates front-end DIC in series with ADRC, reducing the adverse effect of control input distortion on disturbance rejection. Under the same external load impact, DIC-ADRC further suppresses the maximum tracking error to 0.315 mm and shortens the recovery time to 0.080 s, corresponding to reductions of 59.4% and 62.4% relative to PID, respectively. DIC-IADRC achieves the best disturbance rejection performance, with the maximum tracking error and recovery time further reduced to 0.272 mm and 0.039 s, respectively. Compared with PID, these two indicators are reduced by 64.9% and 81.6%, respectively, confirming the improved robustness and convergence performance of the proposed method.

4.3. Sinusoidal Signal Response

To verify tracking performance for continuous time-varying signals, a sinusoidal displacement reference with an amplitude of 25 mm and a frequency of 0.8 Hz is applied. The maximum deviation, MAE, and STD are adopted as tracking performance indices. The maximum deviation refers to the largest absolute error between the commanded and

measured displacements over the tracking period, which characterizes the worst-case tracking accuracy. The reduction rate of maximum deviation relative to PID is computed as the percentage decrease in maximum deviation with respect to PID. Figure 9 and Table 3 present the tracking results.

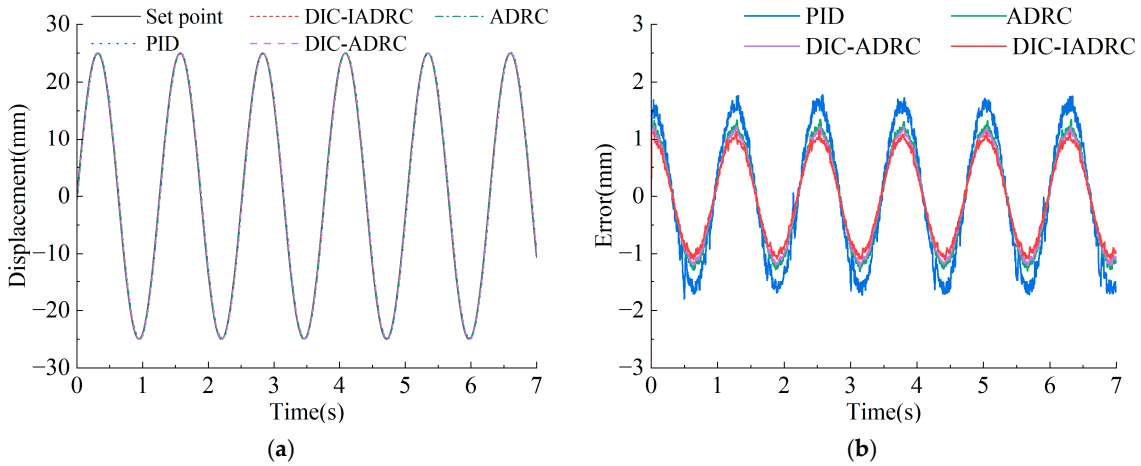


Figure 9. Experimental results of sinusoidal displacement tracking. (**a**) Sinusoidal displacement tracking curve; (**b**) sinusoidal displacement tracking error curve.

Table 3. Comparison of sinusoidal displacement tracking performance metrics.

Performance Metric	PID	ADRC	DIC-ADRC	DIC-IADRC
Maximum deviation (mm)	1.802	1.349	1.242	1.158
MAE (mm)	1.028	0.771	0.728	0.653
Error STD (mm)	1.145	0.859	0.812	0.727
Max. deviation reduction (%)	–	25.1	29.1	35.7

As shown in Table 3, under continuous sinusoidal signal tracking, the performance differences among the four control strategies follow the same pattern as in the step experiments. During sinusoidal tracking, the system is most significantly affected by the flow dead zone during velocity zero-crossing reversals, where the control input must traverse the dead zone to change direction, which tends to produce large tracking lag. PID control lacks active compensation for dead-zone nonlinearity; its maximum deviation reaches 1.802 mm, MAE is 1.028 mm, and error STD is 1.145 mm, with particularly pronounced tracking errors at zero-crossing reversals. Standard ADRC estimates and feedforward-compensates the total disturbance through the ESO, reducing the maximum deviation to 1.349 mm (25.1% lower than PID), with MAE and error STD reduced to 0.771 mm and 0.859 mm, respectively. However, because it treats the structural dead-zone nonlinearity as a general disturbance, noticeable tracking lag remains at velocity reversals. DIC-ADRC compensates for the dead-zone nonlinear distortion at the input through DIC, effectively reducing the velocity lag caused by the flow dead zone during reversal. Its maximum deviation, MAE, and error STD decrease to 1.242 mm, 0.728 mm, and 0.812 mm, respectively. DIC-IADRC further improves the tracking performance, reducing these three indicators to 1.158 mm, 0.653 mm, and 0.727 mm, respectively. Compared with PID, the maximum deviation of DIC-IADRC is reduced by 35.7%, while MAE and error STD are also substantially reduced, demonstrating its superior tracking accuracy under continuous sinusoidal reference inputs.

Compared with existing dead-zone compensation-based disturbance observer schemes, the proposed DIC-IADRC faces several practical challenges. First, accurate dead-zone parameter identification is required to construct the inverse compensator. Variations in load pressure, oil temperature, chamber volume, and motion direction may alter the dead-zone characteristics and introduce compensation errors. Second, the compensator and HOSMO require coordinated parameter tuning to balance compensation accuracy, disturbance estimation speed, and noise sensitivity. The proposed framework is applicable to both pump-controlled and valve-controlled hydraulic cylinder systems with identifiable input-side dead-zone nonlinearities. For different system configurations, the dead-zone model and inverse compensator need to be established according to their respective physical characteristics. Further investigations are required to evaluate its adaptability under widely varying operating conditions.

5. Conclusions

In this study, a DIC-IADRC strategy is proposed for the position control of pump-controlled hydraulic die cushions under flow dead-zone nonlinearity, parameter variations, and external load disturbances. The flow dead-zone mechanism is analyzed by considering leakage across multiple piston-pump friction pairs and oil compressibility in the high-pressure chamber. The resulting model describes the main factors influencing the dead-zone characteristics, while the actual dead-zone parameters are identified experimentally under a 10 kN load for constructing the smooth inverse compensator.

The proposed DIC-IADRC combines dead-zone compensation with residual disturbance observation. By introducing the compensation error into the HOSMO as a known input, the dead-zone nonlinearity is compensated separately, while the remaining compensation uncertainty is included in the lumped disturbance. The FFTD and NLSEF further improve the dynamic response and tracking performance.

On the constructed experimental platform, step tracking, sudden-load disturbance rejection, and sinusoidal tracking experiments are conducted to evaluate the proposed method, with PID, standard ADRC, and DIC-ADRC as comparative methods. Compared with PID, DIC-IADRC reduces the step overshoot, steady-state MAE, maximum disturbance tracking error, and maximum sinusoidal tracking deviation by 79.4%, 83.6%, 64.9%, and 35.7%, respectively. It also outperforms standard ADRC in all three experiments. Compared with DIC-ADRC, the proposed method further reduces the step overshoot, steady-state MAE, and disturbance recovery time by 31.8%, 42.9%, and 51.3%, respectively. These results demonstrate the effectiveness of the proposed strategy in improving position tracking and disturbance rejection.

Author Contributions: Methodology, S.H. and Z.D.; investigation, Z.M. and Y.L.; resources, Z.D., G.Y., H.Z., and C.A.; writing—review and editing, S.H., Z.M., H.A., and K.Z. All authors have read and agreed to the published version of the manuscript.

Funding: This work was supported by the Science Research Project of Hebei Education Department (CXY202403), the Natural Science Foundation of Xinjiang Uygur Autonomous Region (2025D01E18), and the Funds for Local Scientific and Technological Development under the Guidance of the Central Government (CXZX2026005).

Data Availability Statement: Data will be made available on request.

Conflicts of Interest: The authors declare that they have no known competing financial interests or personal relationships that could have appeared to influence the work reported in this paper.

References

1. Najafi, F.; Fathi, M.; Saadat, M. Dynamic modelling of servo pneumatic actuators with cushioning. *Int. J. Adv. Manuf. Technol.* **2009**, *42*, 757–765. [CrossRef]
2. He, S.; Dong, Z.K.; Liao, Y.; An, H.J.; Feng, X.; Ai, C.; Chen, G.X.; Yan, G.S. Adaptive backstepping sliding mode control for blank holder force with surplus force compensation in pump-controlled hydraulic die cushions. *Control Eng. Pract.* **2026**, *171*, 106868. [CrossRef]
3. Shu, S.; Wu, S.; Jiao, Z.X. Optimal trajectory tracking control of servo hydraulic die cushion based on adaptive iterative learning control. *Proc. Inst. Mech. Eng. Part C J. Mech. Eng. Sci.* **2026**, *240*, 2944–2964. [CrossRef]
4. Gao, B.Z.; Li, X.; Zeng, X.H.; Chen, H. Nonlinear control of direct-drive pump-controlled clutch actuator in consideration of pump efficiency map. *Control Eng. Pract.* **2019**, *91*, 104110. [CrossRef]
5. Helian, B.; Chen, Z.; Yao, B.; Lyu, L.T.; Li, C. Accurate motion control of a direct-drive hydraulic system with an adaptive nonlinear pump flow compensation. *IEEE/ASME Trans. Mechatron.* **2020**, *26*, 2593–2603. [CrossRef]
6. Shi, S.Y.; He, Z.L.; Zeng, D.B.; Huang, P.; Lin, G. Identification and modeling of a servo pump-controlled hydraulic system. *IEEE/ASME Trans. Mechatron.* **2025**, *30*, 2551–2561. [CrossRef]
7. Zhu, Y.K.; Qiao, J.Z.; Zhang, Y.M.; Guo, L. High-precision trajectory tracking control for space manipulator with neutral uncertainty and deadzone nonlinearity. *IEEE Trans. Control Syst. Technol.* **2019**, *27*, 2254–2262. [CrossRef]
8. Zheng, J.M.; Zhao, S.D.; Wei, S.G. Application of self-tuning fuzzy PID controller for a SRM direct drive volume control hydraulic press. *Control Eng. Pract.* **2009**, *17*, 1398–1404. [CrossRef]
9. Zhang, Z.; Guo, Y.N.; Gong, D.W.; Zhu, S. Hybrid extended state observer-based integral sliding mode control of the propulsion for a hydraulic roofbolter. *Control Eng. Pract.* **2022**, *126*, 105260. [CrossRef]
10. Li, J.Y.; Zhang, S.D.; Du, X.Y.; Wang, E.C. Improved sliding-mode control for high-dynamic-accuracy EHA in exoskeleton joint. *Adv. Theory Simul.* **2026**, *9*, e20260026. [CrossRef]
11. Wang, B.L.; Cai, Y.; Song, J.C.; Sepehri, N. LuGre model-based robust adaptive control for a pump-controlled hydraulic actuator experiencing friction. *Trans. Inst. Meas. Control* **2024**, *46*, 1845–1857. [CrossRef]
12. Huang, Z.; Xu, Y.; Ren, W.; Fu, C.; Cao, R.; Kong, X.; Li, W. Design of position control method for pump-controlled hydraulic presses via adaptive integral robust control. *Processes* **2022**, *10*, 14. [CrossRef]
13. Cho, S.H.; Burton, R. Position control of high performance hydrostatic actuation system using a simple adaptive control (SAC) method. *Mechatronics* **2011**, *21*, 109–115. [CrossRef]
14. Wang, Y.; Wang, M.K.; Fu, J.; Fu, Y.L. Adaptive control of an aerospace electrohydrostatic actuator with a constant-torque variable-displacement pump. *J. Aerosp. Eng.* **2022**, *35*, 04022028. [CrossRef]
15. Sekban, H.T.; Can, K.; Basci, A. Model-based dynamic fractional-order sliding mode controller design for performance analysis and control of a coupled tank liquid-level system. *Adv. Electr. Comput. Eng.* **2020**, *20*, 93–100. [CrossRef]
16. Bu, D.B.; Ahn, K.K.; Truong, D.Q.; Park, H.S. Integrated model-based backstepping control for an electro-hydraulic system. *Int. J. Precis. Eng. Manuf.* **2016**, *17*, 621–631. [CrossRef]
17. Ahn, K.K.; Nam, D.N.C.; Jin, M. Adaptive backstepping control of an electrohydraulic actuator. *IEEE/ASME Trans. Mechatron.* **2014**, *19*, 987–995. [CrossRef]
18. Chen, G.X.; Liu, H.L.; Jia, P.S.; Qiu, G.T.; Yu, H.H.; Yan, G.S.; Ai, C.; Zhang, J. Position output adaptive backstepping control of electro-hydraulic servo closed-pump control system. *Processes* **2021**, *9*, 2209. [CrossRef]
19. Kim, H.M.; Park, S.H.; Song, J.S.; Kim, J.S. Robust position control of electro-hydraulic actuator systems using the adaptive back-stepping control scheme. *Proc. Inst. Mech. Eng. Part I J. Syst. Control Eng.* **2010**, *224*, 737–746. [CrossRef]
20. Yang, X.W.; Ge, Y.W.; Deng, W.X.; Yao, J.Y. Observer-based motion axis control for hydraulic actuation systems. *Chin. J. Aeronaut.* **2023**, *36*, 408–425. [CrossRef]
21. Qin, Q.T.; Li, Y.H.; Quan, L.; Yang, L.M. An adaptive robust impedance control considering energy-saving of hydraulic excavator boom and stick systems. *IEEE/ASME Trans. Mechatron.* **2022**, *27*, 1928–1936. [CrossRef]
22. Yang, X.W.; Ge, Y.W.; Deng, W.X.; Yao, J.Y. Precision motion control for electro-hydraulic axis systems under unknown time-variant parameters and disturbances. *Chin. J. Aeronaut.* **2024**, *37*, 463–471. [CrossRef]
23. Chen, X.Y.; Huang, X.; Guo, J.K.; Lin, F.L.; Jia, L.H.; Yang, H.Y.; Zhu, Y. Automation on electro-hydraulic rotation system of segment assembly machine in tunnel boring. *Front. Mech. Eng.* **2025**, *20*, 40. [CrossRef]
24. Zong, H.Z.; Yang, Z.X.; Yu, X.; Zhang, J.H.; Ai, J.K.; Zhu, Q.X.; Wang, F.; Su, Q.; Xu, B. Active disturbance rejection control of hydraulic quadruped robots rotary joints for improved impact resistance. *Chin. J. Mech. Eng.* **2024**, *37*, 103. [CrossRef]
25. Huang, Y.; Xue, W.C. Active disturbance rejection control: Methodology and theoretical analysis. *ISA Trans.* **2014**, *53*, 963–976. [CrossRef] [PubMed]
26. Li, J.; Zhang, L.Y.; Li, S.Q.; Mao, Q.B.; Mao, Y. Active disturbance rejection control for piezoelectric smart structures: A review. *Machines* **2023**, *11*, 174. [CrossRef]

27. Zheng, Q.; Gao, Z.Q. Predictive active disturbance rejection control for processes with time delay. *ISA Trans.* **2014**, *53*, 876–883. [CrossRef] [PubMed]
28. Chen, S.; Li, X.J.; Xue, W.C.; Zhong, S.; Pi, Y.J.; Huang, Y. On comparison of modified ADRCs for nonlinear uncertain systems with time delay. *Sci. China Inf. Sci.* **2018**, *61*, 072203. [CrossRef]
29. Jiang, H.Y.; Ling, Z.F.; Zhou, F.Q.; Sun, M.W.; Liu, H.; Xu, L.L.; Yao, Y.M.; Ouyang, X.P.; Yang, H.Y. Adaptive dead zone compensation control method for electro-hydrostatic actuators under low-speed conditions. *Chin. J. Mech. Eng.* **2024**, *37*, 5. [CrossRef]
30. Wang, F.; Chen, G.X.; Liu, H.L.; Yan, G.S.; Zhang, T.G.; Liu, K.Y.; Liu, Y.; Ai, C. Research on position control of an electro-hydraulic servo closed pump control system. *Processes* **2022**, *10*, 1674. [CrossRef]
31. Yang, E.R.; Zheng, D.Y.; Zhao, J.; Cai, Y.Q.; Peng, B.; Zhang, L.Y.; Li, G. Active disturbance rejection super-twisting integral sliding mode control of wrist rehabilitation robot driven by foldable air bag. *Control Eng. Pract.* **2025**, *164*, 106305. [CrossRef]
32. Zhao, Y.; Liu, Y.; Zhang, H.; Zhao, N.; Shi, Y. Funnel-based predefined-time output feedback fuzzy adaptive event-triggered platoon control for heterogeneous vehicles. *IEEE Internet Things J.* **2026**, *13*, 39672–39682. [CrossRef]

Disclaimer/Publisher's Note: The statements, opinions and data contained in all publications are solely those of the individual author(s) and contributor(s) and not of MDPI and/or the editor(s). MDPI and/or the editor(s) disclaim responsibility for any injury to people or property resulting from any ideas, methods, instructions or products referred to in the content.